American Mineralogist, Volume 97, pages 864–871, 2012

Experimental investigation of smectite interaction with metal iron at 80 °C: Structural characterization of newly formed Fe-rich phyllosilicates

Bruno Lanson,[1,*] Sébastien Lantenois,[2] Peter A. van Aken,[3] Andreas Bauer,[4] and Alain Plançon[2]

[1]ISTerre, Grenoble University, CNRS, F-38041 Grenoble, France
[2]Institut des Sciences de la Terre d'Orléans (ISTO), Orléans University, CNRS, F-45071 Orléans, France
[3]Stuttgart Center for Electron Microscopy, Max Planck Institute for Intelligent Systems, D-70569 Stuttgart, Germany
[4]Institut für Nukleare Entsorgung, Karlsruhe Institute of Technology, D-76021 Karlsruhe, Germany

Abstract

Interactions between metallic iron and clay minerals have been extensively studied under low-temperature anoxic conditions owing to their potential impact on the long-term safety of high-level nuclear waste disposal in deep geological repositories. To complement the studies investigating the destabilization mechanisms and rates of various initial clay minerals, the prediction of the storage long-term performance requires a comprehensive characterization of the reaction products. The Fe-rich 1:1 phyllosilicates resulting from interactions at 80 °C and in the absence of O_2 between metallic iron and smectites with contrasting compositions are thus characterized chemically and structurally using various experimental techniques (X-ray and electron diffractions, infrared, energy-dispersive, and electron energy loss spectroscopies, and high-resolution electron microscopy). Cronstedtite and odinite are the two Fe-rich 1:1 phyllosilicates formed under the experimental conditions investigated, both species differing from their relative contents and the average valence state of structural Fe. No parental link has been evidenced between the two minerals despite their contrasting crystal morphologies and thermodynamical predictions. The formation of the 1:1 phyllosilicates apparently results from the destabilization of the initial smectite through the formation of an intermediate gel.

Keywords: Iron-clay, nuclear waste, smectite, serpentine, berthierine, cronstedtite, odinite

Introduction

Multi-barrier concepts are envisaged in most countries for the long-term underground storage of high- and intermediate-level and/or long-lived nuclear waste. To prevent the release of radionuclides to the biosphere, metallic containers filled with nuclear waste are possibly placed in an engineered confinement barrier, which is itself surrounded by the geological barrier. Depending on the countries, canisters could be made of carbon steel, stainless steel, or copper, whereas bentonite is universally considered as the major component of engineered barriers (Gates et al. 2009). Bentonite's main constituent, smectite, combines swelling and self-healing abilities with high cation retention and surface sorption capacities, thus ensuring mechanical stability, low hydraulic conductivity, and minimum release of radionuclides. In some concepts, such as the one currently envisaged by the French agency Andra, the engineered barrier is absent, but smectite is present however as a major component of the geological barrier. However, the safety of the whole concept depends strongly on the long-term stability of smectite in response to thermal and chemical perturbations induced by the waste storage. The formation of non-swelling phyllosilicates and/or of phyllosilicates with low-sorption capacity at the expense of smectite would be detrimental to the storage performance. For example, a wealth of literature has been devoted to the impact of the high-pH plume resulting from cement alteration on the clay mineralogy of both engineered and geological barriers (Chermak 1992, 1993; Claret et al. 2002; Ramirez et al. 2005; Bauer et al. 2006; Charpentier et al. 2006; Sanchez et al. 2006; Devol-Brown et al. 2007; Savage et al. 2007; Cuisinier et al. 2008; Honty et al. 2010).

Similarly, metallic iron-clay, and more specifically metallic iron-smectite, interactions have been thoroughly investigated both experimentally and through thermodynamical modeling. Both approaches are consistent in that they report the destabilization of dioctahedral smectite under neutral to alkaline pH conditions if the metallic iron:clay ratio exceeds a threshold value (~1:5 at 80 °C, Lantenois et al. 2005; Bildstein et al. 2006; Wilson et al. 2006b; Perronnet et al. 2008; Mosser-Ruck et al. 2010; Osacky et al. 2010; Savage et al. 2010; De Combarieu et al. 2011). However, the influence of the chemical composition of smectite, and more especially of its iron content, remains controversial as thermodynamical modeling predicts a higher stability for iron-rich dioctahedral smectite (nontronite; Wilson et al. 2006b) in contradiction with experimental evidence (Lantenois et al. 2005). At temperatures exceeding 150 °C, experimental metallic iron-smectite interactions lead to the formation of iron-rich smectites (di- and/or trioctahedral) and/or of chlorite (Guillaume et al. 2003, 2004; Charpentier et al. 2006; Wilson et al. 2006a; Mosser-Ruck et al. 2010). Over the 50–100 °C range predicted

* E-mail: bruno.lanson@obs.ujf-grenoble.fr

0003-004X/12/0506–864$05.00/DOI: http://dx.doi.org/10.2138/am.2012.4062

within the waste disposal site, reaction products appear to be different with the systematic formation of non-swelling iron-rich 1:1 phyllosilicates under anaerobic conditions (Lantenois 2003; Perronnet 2004; Habert et al. 2006; Wilson et al. 2006a; Perronnet et al. 2008; Mosser-Ruck et al. 2010; Osacky et al. 2010; De Combarieu et al. 2011). The precipitation of such an iron-rich 1:1 phyllosilicate is consistent with thermodynamical modeling of metallic iron-smectite interactions under anaerobic conditions (Bildstein et al. 2006; Wilson et al. 2006b; Savage et al. 2010). It is expected to have a detrimental effect on porosity and on fluid circulation within the clay barrier (Bildstein et al. 2006).

Taking the potential compositional variability of the 1:1 phyllosilicates into account for these calculations leads to contrasting stability domains or sequences of formation for different species (Savage et al. 2010). Despite its key influence on the overall performance and safety of the repository, the actual nature of the newly formed phyllosilicates has attracted little attention in experimental studies of metallic iron-smectite interactions. These phyllosilicates are commonly identified as "berthierine-like" with experimental data often limited to their Si:Fe ratio. The present study thus aims at a thorough characterization of the crystal chemistry of the iron-rich phyllosilicates formed as the result of metallic iron-smectite interactions in low-temperature anoxic conditions that prevail in a nuclear waste repository. This experimental study was performed with three initial smectites, namely one montmorillonite, one beidellite, and one nontronite, to cover the common compositional range of dioctahedral smectites. Due to the incomplete destabilization of the reactants, and to the polyphasic character of reaction products, different chemical [energy dispersive spectroscopy (EDS), electron energy loss spectroscopy (EELS)], and structural [(X-ray and electron diffractions, infrared spectroscopy (IR), high-resolution transmission electron microscopy (HR-TEM)] probes were used. When possible, a microscopic probe was used to obtain information on individual particles.

Materials and methods

Materials

Three natural smectite-rich samples [SbId beidellite and SWy-2 montmorillonite from the Source Clays Repository of the Clay Minerals Society (CMS), and Garfield nontronite] were selected for the experiments both for their contrasting destabilization rates (Lantenois et al. 2005) and their contrasting crystal chemistry

$Na_{0.08}K_{0.08}Ca_{0.10}[Si_{3.71}Al_{0.29}][Al_{1.80}Fe^{3+}_{0.12}Mg_{0.08}]O_{10}(OH)_2$,
$Na_{0.14}K_{0.01}Ca_{0.05}[Si_{3.95}Al_{0.05}][Al_{1.56}Fe^{3+}_{0.21}Mg_{0.23}]O_{10}(OH)_2$, and
$Na_{0.09}K_{0.04}Ca_{0.19}[Si_{3.51}Al_{0.49}][Al_{0.11}Fe^{3+}_{1.86}Mg_{0.02}]O_{10}(OH)_2$

for SbId beidellite, SWy-2 montmorillonite, and Garfield nontronite, respectively (Gates et al. 2002; Lantenois et al. 2005). Samples were lightly ground in an agate mortar to increase their reactivity, but were neither size-fractionated nor purified despite the likely influence of accessory minerals on smectite reactivity. Metallic iron powder (10 µm size at maximum) from Merck and deionized water (resistivity >18 MΩ cm^{-1}) were used for the experiments.

Natural chlorite CCa-2 (ripidolite from the CMS Source Clays Repository), $[Si_{2.67}Al_{1.33}][Al_{1.24}Fe^{3+}_{0.47}Fe^{2+}_{1.51}Mg_{2.75}Ti_{0.01}Mn_{0.01}]O_{10}(OH)_8$ (Brandt et al. 2003); berthierine from the Jurassic ironstone (Isle of Raasay, U.K., A. Bauer, personal collection), $[Si_{1.11}Al_{0.89}][Al_{0.89}Fe^{2+}_{2.10}Mg_{0.01}]O_5(OH)_4$ (Toth and Fritz 1997); and a synthetic Si-Al-Fe gel were used for comparison with the reaction products of iron-clay interactions. The synthetic gel phase was prepared following a method adapted from Hamilton and Henderson (1968) using tetraethylorthosilicate (TEOS), $Al(NO_3)_3$, $Fe(NO_3)_3$, HNO_3, NH_4OH, and ethanol, as described by Lantenois et al. (2005).

Experimental protocols

Clay powder and metallic iron powder were mixed in a 1:1 weight ratio to enhance interactions between iron and clay particles. The large content of metallic iron aimed also at promoting reducing conditions during the experiments. Thirty milliliters of water were added to the solid mixture (1.2 g). Samples were prepared in a MBraun glove box filled with Ar gas, and equipped with Cu catalysts to eliminate O_2, and an MBraun O_2 control system. The partial pressure of O_2 was <1 ppm during sample preparation. Deionized water was degassed with Ar for 1 h prior to its introduction in the glove box and all products were allowed to stay in the glove box for 24 h to equilibrate with the glove box atmosphere. Initial suspensions were then filled in 40 mL Nalgene reactors. Because these reactors are oxygen porous, a "double enclosure system" was used with the Nalgene reactors being inserted into larger polytetrafluoroethylene reactors containing metallic iron powder, $FeSO_4$, and deionized water. Oxygen entering polytetrafluoroethylene reactors was eliminated from its reaction with both metallic and ferrous iron (Lantenois et al. 2005). All reactors were tightly closed within the glove box and subsequently heated at 80 °C (±1 °C) for 45 days outside of the glove box. At the end of the reactions, the reactors were cooled down to room temperature and opened in air. The solid fraction was separated by filtration at 0.45 µm, dried at 80 °C overnight, and finally ground in an agate mortar.

For SWy-2, magnetic (metallic iron, magnetic iron oxides) and non-magnetic reaction products were separated to ease the characterization of the latter fraction. For this purpose, reaction products were mixed with deionized water in a beaker and sonicated for 5 min. The resulting suspension was then mechanically stirred. After 15 min, the magnetic stirrer was removed and rinsed to eliminate magnetic particles. Mechanical stirring was repeated (up to 15 times) until no magnetic particles were visible on the stir bar. The non-magnetic fraction was then dried at 80 °C in air for 48 h. This non-magnetic fraction was then ion-exchanged at room temperature using a 1.0 mol/L NaCl solution. The suspension was mechanically shaken in this saline solution for 12 h before separation of the solid fraction by centrifugation and addition of fresh saline solution. The exchange step was repeated five times to ensure the complete saturation of residual smectite interlayers. Excess salt was eliminated with one cycle of washing in ethanol, including sedimentation and removal of the supernatant, and one cycle in deionized water. The resulting solid was then dialyzed in deionized water for five days, collected, and placed in a beaker. After 30 min of sedimentation, the stable suspension, which essentially contains smectite was eliminated to concentrate the non-magnetic reaction products of the iron-clay interactions. This purification process was not possible for SbId beidellite and Garfield nontronite.

Sample characterization

Powder XRD patterns were recorded in transmission geometry using Co$K\alpha$ radiation (35 mA, 35 kV) to avoid fluorescence from iron, and 0.5 mm diameter Lindemann glass capillaries. The use of an INEL CPS 120 diffractometer equipped with a curved position sensitive detector allowed recording simultaneously the diffracted intensity over the 4–50 °2θ range (total data collection time: 1–2 h) with a step size of 0.03° after correction for its non-linearity (Roux and Volfinger 1996). XRD patterns were calculated as described by Plançon (2002, 2003).

Infrared spectra were recorded with a 2 cm^{-1} resolution over the 650–4000 cm^{-1} range using a Nicolet Magna-IR Fourier transform (FT) spectrometer equipped with a Globar SiC source and a DTGS (deuterated triglycine sulfate) detector. The spectrometer was purged with dry air prior to data collection to minimize the amount of atmospheric H_2O. The sample was finely ground in an agate mortar, 0.5 mg of the resulting powder being mixed to 150 mg of KBr previously dried at 120 °C for 24 h. The mixture was homogenized and pressed in an evacuable die to prepare a 12 mm diameter pellet.

High-resolution transmission electron microscopy imaging and energy-dispersive spectroscopy chemical analyses were performed with a JEOL 2000 FX TEM operated at 200 kV. The microscope was equipped with a double-tilt (±30°) HR specimen holder and a Si-Li Oxford EDS detector with a 30 nm^2 super atmospheric thin window. Spectra were collected for 60 s (with an idle time ranging from 0 to 10%) on a 10 nm diameter surface area under convergent beam. Semi-quantitative analyses were obtained from the TEMQUANT-ISIS software developed by Oxford Instruments. Highly diluted aqueous suspensions of the samples were dried on a copper mesh grid for imaging and analysis.

Electron energy-loss spectroscopy data were recorded using a Philips CM 12 TEM fitted with a Gatan PEELS 666 parallel electron spectrometer. The TEM was equipped with a single-crystal LaB_6 cathode and operated at 120 kV with an illumination angle $2\alpha = 5.2$ mrad and a collection angle $2\beta = 14.0$ mrad. The entire system (TEM/EELS) yielded a typical energy spread of 0.8 eV. Instrumental details

are provided by van Aken et al. (1998) and van Aken and Liebscher (2002) together with the evaluation of EELS data, which includes corrections for dark current and noise and for channel-to-channel gain variations of the detector. Background subtraction was performed with an inverse power-law function. Multiple scattering contributions and tailing effects of the zero-loss peak were deconvoluted by the Fourier-ratio technique (Egerton 1996) using the corresponding low-loss spectra from the same specimen region. Finally the $Fe^{3+}/\Sigma Fe$ ratio was determined from the intensity ratio of Fe^{3+} L_3 and Fe^{2+} L_2 lines integrated over the 708.5–710.5 and the 719.7–721.7 eV ranges, respectively (van Aken et al. 1998).

Results and discussion

Identification of reaction products

As reported by Lantenois et al. (2005), the reactivity of the three samples differs according to the presence of iron, essentially as a function of their octahedral iron content and of the location (tetrahedral vs. octahedral) of the isomorphous substitutions. After 45 days of interactions with metallic iron, the 02,11 band reflection of Garfield nontronite has almost completely disappeared (Fig. 1), indicating a reaction rate of ~90%. In contrast, this band is still clearly visible in the XRD patterns of reacted SbId and SWy-2 whose destabilization rates are lower (60 and 50%, respectively). As noted by Lantenois et al. (2005), the possible bias due to the overlap of the newly formed phyllosilicates with the 02,11 band (see below) was minimal owing to both the positional shift and the low intensity of the latter peak resulting from their content of structural Fe. Despite this reactivity contrast, the reaction products appear to be the same for all samples investigated in the present study. As described by Lantenois et al. (2005), magnetite exhibiting cubic crystal habits was formed systematically as a result of metallic iron-smectite interactions (Figs. 1 and 2a). The completely oxidized lepidocrocite (γ-FeOOH) was observed only in reacted SbId (Fig. 1b).

To enhance the characterization of the newly formed phyllosilicates as much as possible, the magnetic phases (residual metallic iron and magnetite) and the initial smectite (Fig. 2b) were removed from reacted SWy-2. Following this treatment, no magnetic phases were detected anymore with XRD (Fig. 3), whereas the 001 reflection and 02,11 and 20,13 bands of montmorillonite remained visible at 12.5, 4.47, and 2.53 Å, respectively (8.2, 23.1, and 41.4 °2θ Co$K\alpha$, respectively). In addition to the basal 001 and 002 reflections, which were visible at ~7.1 and 3.55 Å (~14.5 and 29.2 °2θ Co$K\alpha$, respectively) in the XRD pattern of the whole reacted SWy-2 (Fig. 1c), the newly formed phyllosilicates exhibited reflections at 2.72 and 2.44 Å (38.4 and 43.0 °2θ Co$K\alpha$, respectively), typical for 1:1 phyllosilicates (serpentine or kaolinite type; Moore and Reynolds 1997). In reacted SWy-2 and SbId, this phyllosilicate was present both as thick crystals hexagonally shaped within the layer plane (Figs. 2c and 2d) and as thinner crystals with no distinct shape within the layer plane (Fig. 2e). These two major habits are hereafter referred to as particles of type I and II, respectively. A unique type of particles with intermediate crystal thickness was observed for reacted Garfield nontronite. Both lattice-fringe images obtained perpendicular to the layer plane, and selected-area electron diffraction (SAED) patterns confirmed the ~7 Å periodicity along the **c*** axis for all types of particles (Fig. 4). Despite their related crystal structure the two types of particles have distinct chemical compositions (Table 1), Fe and Si being always the major elements with minor contents of Al, thus suggesting a serpentine structure. Compared to Type I, the Type II particles had higher Si:Fe (0.97–1.13 compared to 0.44–0.48) and lower Si:Al (1.56–2.65 compared to 1.80–4.25) ratios, the contents of alkali Earth elements being systematically marginal. In contrast with Si:Fe, the Si:Al ratio appeared to be controlled by that of the initial smectite composition, ranging from 1.56–1.80 (SbId), to 2.65–4.24 (SWy-2), and to 5.83 (Garfield, Table 1), when the ratios in the initial materials were 1.77, 2.45, and 5.85, respectively. The formation of elementary "bricks" as the result of the initial smectite destabilization and the subsequent crystallization of the new phyllosilicate from these bricks is possibly responsible for the similar Si:Al ratios in the two species.

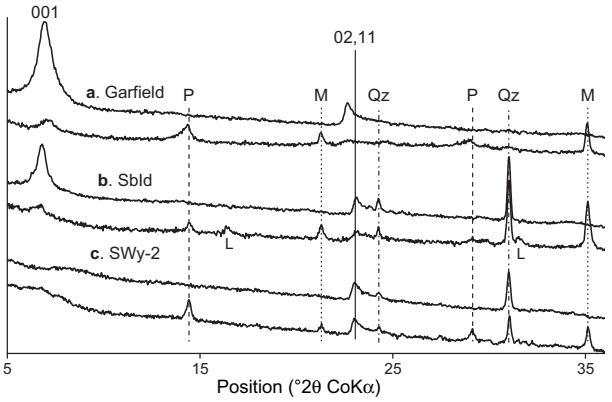

Figure 1. XRD patterns of initial (top) and reacted (bottom) smectite samples. The 001 reflection and 02,11 band (solid line) of smectite are identified together with quartz (Qz, dotted-dashed line) impurity when present. Newly formed magnetite (M, dotted lines), lepidocrocite (L), and phyllosilicates (P, dashed lines) are also indicated.

Finally, the XRD pattern collected on the purified fraction of reacted SWy-2 revealed a broad hump centered at ~30 °2θ Co$K\alpha$ that can be attributed to the presence of a Si-Al-Fe gel (Fig. 3a). Such a gel phase was observed systematically under the TEM (Fig. 2f), and the diffraction signature of a synthetic gel of similar composition reproduces the observed diffuse maximum.

Newly formed phyllosilicate: Crystal chemistry

Although the newly formed clay phases systematically exhibit basal XRD reflections at ~7.1 and 3.55 Å (Figs. 1 and 3) consistent with lattice-fringe images and SAED data, the actual periodicity of these phyllosilicates was not unambiguous. The low intensity of 001 and 003 reflections (at 14.1 and 4.70 Å, respectively) calculated for an iron-rich chlorite makes X-ray, and electron, diffraction patterns of both iron-rich serpentine and chlorite akin (Fig. 5), thus hampering their unambiguous differentiation, especially when these phases are not present as pure separates as in the present case study. To overcome this uncertainty, FTIR spectra were collected over the OH stretching domain (3300–3700 cm^{-1}). Over this frequency domain, chlorites exhibit two broad and intense bands at ~3400 and ~3550 cm^{-1} arising from their brucite layers (Farmer 1974; Kodama 1985). Conversely, iron-rich serpentines do not show these two bands and exhibit only diffuse low-intensity vibration bands over

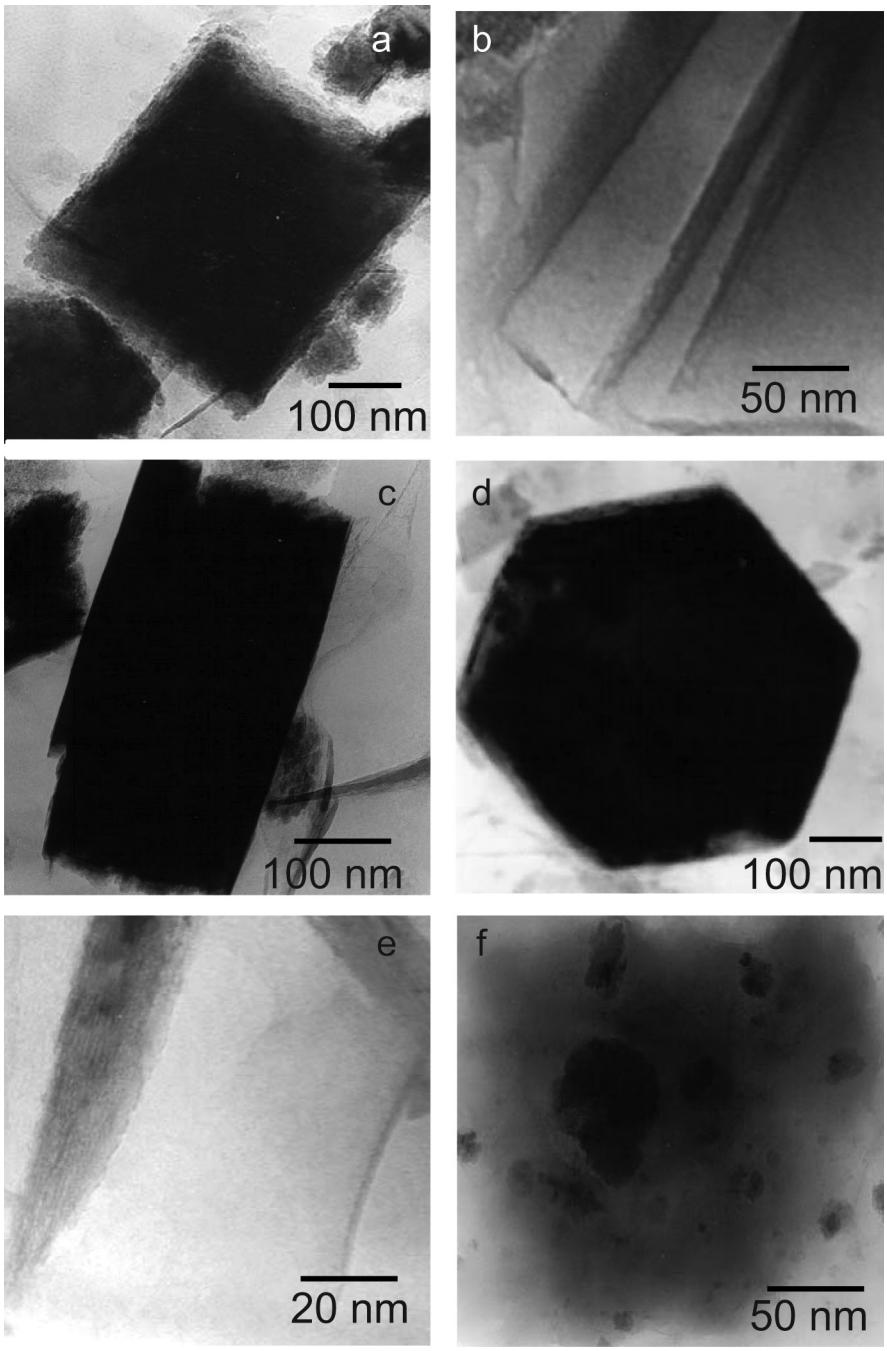

FIGURE 2. Low-resolution TEM images of the reaction products resulting from interactions between metallic iron and SWy-2 montmorillonite. (**a**) Magnetite. (**b**) Unreacted smectite. (**c**, **d**) Newly formed 1:1 phyllosilicate (Type I). (**e**) Newly formed 1:1 phyllosilicate (Type II). (**f**) Si-Al-Fe gel.

the OH stretching domain (Fig. 6b; Kodama 1985), consistent with the signature of reacted and purified SWy-2 (Fig. 6c). This specific signature indicated the absence of a brucite layer in the newly formed phyllosilicates and confirmed thus their serpentine structure.

To fully determine the crystal structure of the newly formed serpentine, the relative proportions of ferric and ferrous iron were needed. Together with the elemental ratio between Si, Al, Fe, and Mg, this parameter is indeed an essential criterion to differentiate Fe-rich serpentine species whose typical compositions are

berthierine: $[Si_{1.3}Al_{0.7}][Al_{0.8}Fe^{3+}_{0.15}Fe^{2+}_{1.75}Mg_{0.20}\square_{0.10}]O_5(OH)_4$ (Brindley 1982; Bailey 1988a);

greenalite: $[Si_{2.0}][Fe^{3+}_{0.45}Fe^{2+}_{1.9}Mg_{0.3}\square_{0.35}]O_5(OH)_4$ (Guggenheim

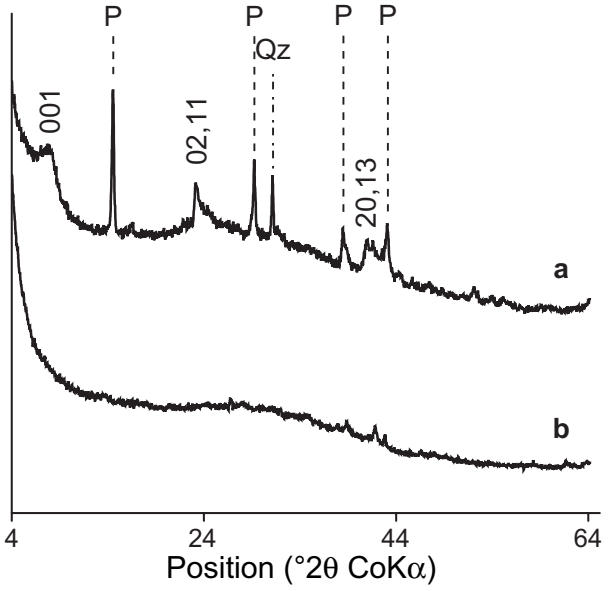

Figure 3. XRD patterns of reacted SWy-2 montmorillonite (**a**) after removal of the magnetic fraction (i.e. remaining metalic iron and magnetite) and of a synthetic Si-Fe-Al gel (**b**). The 001 reflection, 02,11 and 20,13 bands of smectite are identified together with quartz (Qz, dotted-dashed line) impurity, and newly formed phyllosilicates (P, dashed lines).

et al. 1982);

cronstedtite $[Si_{1.25}Fe^{3+}_{0.75}][Fe^{3+}_{0.75}Fe^{2+}_{2.00}Mg_{0.25}\square_{0.00}]O_5(OH)_4$ (Geiger et al. 1983; Kogure et al. 2002; Bailey 1988a);

and odinite: $[Si_{1.85}Al_{0.15}][Al_{0.15}Fe^{3+}_{1.2}Fe^{2+}_{0.35}Mg_{0.7}\square_{0.6}]O_5(OH)_4$ (Bailey 1988a, 1988b).

Because of the multiphasic nature of the reaction products, the ratio between di- and trivalent iron was determined on individual particles by EELS in the TEM (Fig. 7). EELS spectra obtained for each type of particles were similar for SWy-2 and SbId, thus leading to comparable $Fe^{3+}/\Sigma Fe$ ratio (0.44–0.46 and 0.70–0.78, for Type I and II particles, respectively). EELS spectra recorded on type I particles were analogous to those reported by Zega et al. (2003) for cronstedtite resulting from the aqueous alteration of anhydrous Fe,Mg silicates in CM chondrites. Type II particles, which contain less iron were more oxidized (Tables 1–2). The iron oxidation state in newly formed phyllosilicates present in reacted Garfield was close to that of Type I particles.

Combining EELS data with the average chemical compositions determined by EDS, it was possible to calculate the structural formulae for the different types of particles (Table 2; Fig. 8). Octahedral occupancies of all newly formed phyllosilicates were intermediate between di- and tri-octahedral end-members, ranging from 2.25–2.38 (Type II particles and Garfield) to 2.73–2.77 (Type I particles) with large numbers of trivalent Fe [1.1–1.3 per $O_5(OH)_2$] and of ^{VI}Al (0.23–0.61 in Type II particles and Garfield). It is remarkable that in both cases, the resulting positive excess charge of the octahedral sheet compensates almost

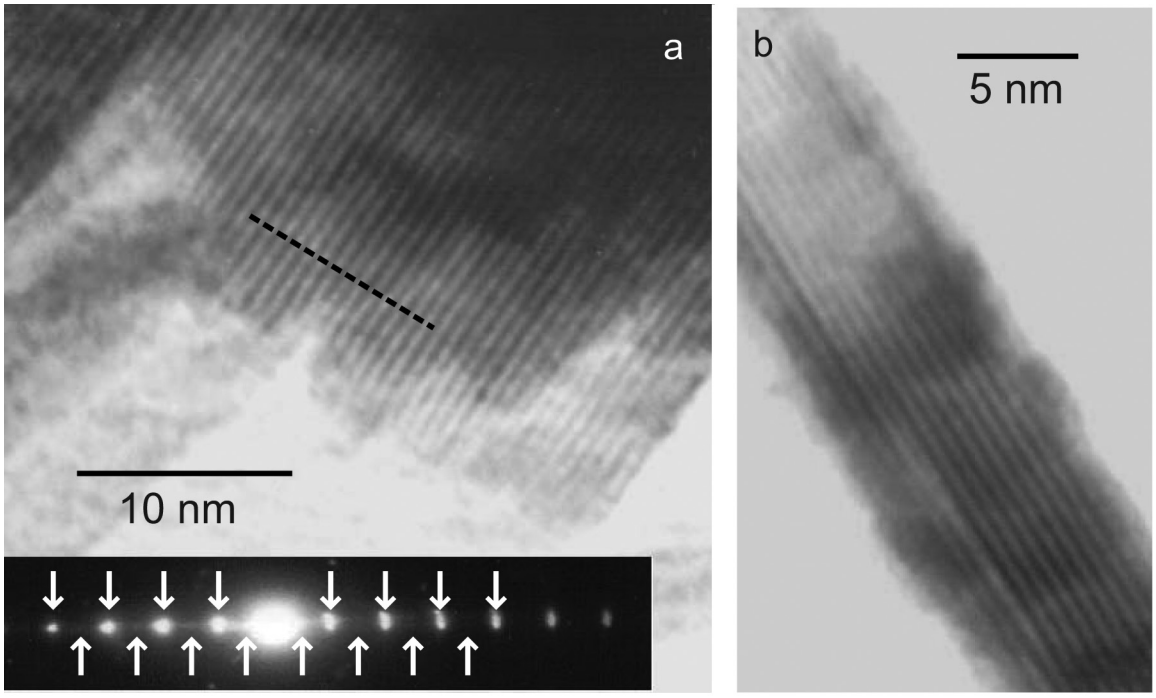

Figure 4. Lattice-fringe TEM images of newly formed 1:1 phyllosilicates of type I. (**a**) Type I. The 10 Å dashed line on the image corresponds to 14 repetitions of the dark-clear motif. On the SAED pattern shown at the bottom of the figure, only reflections corresponding to a ~7 Å periodicity (arrows pointing down) are visible, whereas odd reflections corresponding to a ~14 Å periodicity (arrows pointing up) are absent or weak. (**b**) Type II.

Table 1. Chemical composition of the newly formed phyllosilicate

Sample		Si	Al	Fe	Mg	Ca
Garfield		15.79	2.71	17.76	0.00	0.03
SbId	Type I	10.00	5.54	22.47	0.02	0.10
	Type II	13.90	8.93	14.31	0.00	0.09
SWy-2	Type I	11.27	2.66	23.33	0.26	0.15
	Type II	15.71	5.92	13.88	1.00	0.07

Notes: Chemical compositions were determined by energy-dispersive X-ray fluorescence under the TEM and are expressed as atomic percent. Values correspond to the average of ~10 analyses. The standard deviations were ~40% rel. for Ca and Mg, ~10% rel. for Al, <5% rel. for Si and Fe.

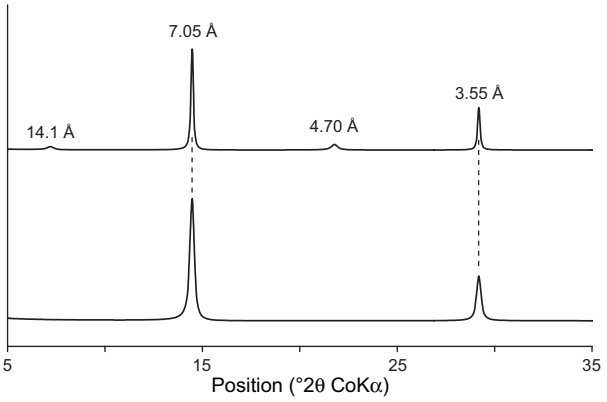

Figure 5. XRD patterns calculated for iron-rich phyllosilicates with a chlorite (2:1:1) ~14 Å periodicity (top) and a serpentine (1:1) ~7 Å periodicity (bottom). Only 00*l* reflections are calculated and common reflections are outlined with dashed lines.

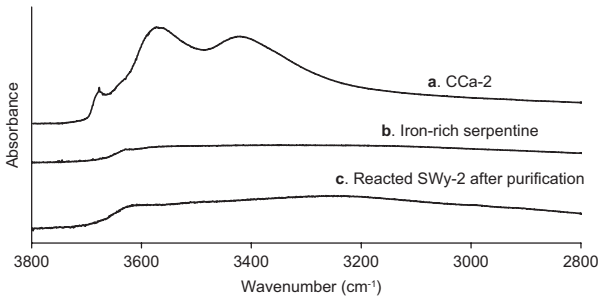

Figure 6. IR infrared spectra of the CCa-2 chlorite (a), of a natural iron-rich serpentine (b), and of reacted SWy-2 montmorillonite after removal of the magnetic fraction (remaining metallic iron and magnetite) and of unreacted smectite (c).

Table 2. Structural formulas of the newly formed 1:1 phyllosilicates

		Tetrahedral sheet				Octahedral sheet					
Sample		Si	Al	Fe^{3+}	charge	Al	Fe^{3+}	Fe^{2+}	Mg	charge	occup.
Garfield		1.91	0.09	0.00	−0.09	0.23	1.10	1.05	0.00	0.09	2.38
SbId	Type I	1.25	0.70	0.05	−0.75	0.00	1.19	1.58	0.00	0.73	2.77
	Type II	1.59	0.41	0.00	−0.41	0.61	1.28	0.36	0.00	0.39	2.25
SWy-2	Type I	1.42	0.34	0.24	−0.58	0.00	1.11	1.59	0.03	0.57	2.73
	Type II	1.83	0.17	0.00	−0.17	0.52	1.13	0.49	0.12	0.17	2.26

Notes: Structural formulas were calculated using the EDS compositions (Table 1) and the Fe^{2+}/Fe^{3+} ratios determined on individual particles by EELS (Fig. 7). Calcium was not considered in the calculation of the structural formulas.

perfectly for the charge deficit of the tetrahedral sheet arising from Al and Fe substitutions for Si (0.58–0.75 in Type I particles, and 0.09–0.41 in Type II particles and Garfield, Table 2). When plotted in a Fe^{2+}-Fe^{3+}-Al^{3+} diagram (Fig. 8), these compositions lie close to cronstedtite (Type I particles and Garfield) and to odinite (Type II particles).

Consistency with previous reports of iron-rich phyllosilicates

The combination of various chemical and structural analyses both on a purified fraction of the reacted metallic iron-smectite mixture and on individual particles of this mixture using the TEM allowed an unprecedented thorough characterization of the crystal chemistry of newly formed iron-rich 1:1 phyllosilicates. It was in particular possible to determine unambiguously the ~7 Å periodicity of this phase using IR spectroscopy, consistent with previous experimental (Lantenois 2003; Perronnet 2004; Wilson et al. 2006a; Perronnet et al. 2008; Mosser-Ruck et al. 2010; Osacky et al. 2010; De Combarieu et al. 2011) and computational (Bildstein et al. 2006; Wilson et al. 2006b; Savage et al. 2010) studies.

Textural evidences suggested that the newly formed 1:1 phyllosilicates precipitated from the maturation of a Si-Al-Fe gel resulting from the destabilization of the initial smectite (Lantenois et al. 2005; Perronnet et al. 2008). This genetic link is suggested also by the positive correlation between the Si:Al

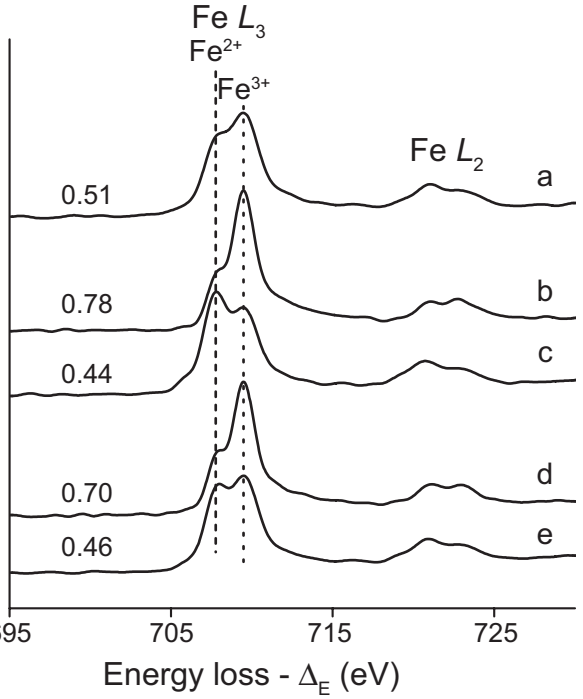

Figure 7. EELS spectra obtained on the newly formed phyllosilicates. (**a**) Reacted Garfield nontronite. (**b**) Reacted SbId beidellite, Type II particles. (**c**) Reacted SbId beidellite, Type I particles. (**d**) Reacted SWy-2 montmorillonite, Type II particles. (**e**) Reacted SWy-2 montmorillonite. Dashed lines outline the position of Fe^{2+} and Fe^{3+} contributions to the spectra.

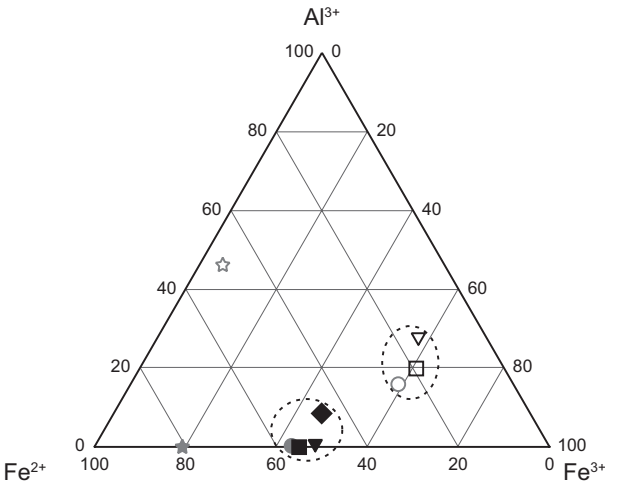

FIGURE 8. Chemical composition of the newly formed 1:1 phyllosilicates plotted in a Al^{3+}-Fe^{3+}-Fe^{2+} ternary diagram. Garfield, SbId, and SWy-2 experiments are represented by diamonds, inverted triangles, and squares, respectively. Open and solid patterns correspond to Type II and I particles, respectively. Typical compositions of berthierine (Brindley 1982; Bailey 1988a), greenalite (Guggenheim et al. 1982), cronstedtite (Geiger et al. 1983; Kogure et al. 2002; Bailey 1988a), and odinite (Bailey 1988a, 1988b) are shown as gray open star, solid star, solid disk, and open disk, respectively.

ratios measured in the initial smectite and the newly formed 1:1 phyllosilicates. Despite this parental relationship, the newly formed 1:1 phyllosilicates exhibit significant heterogeneity within a given reacted sample, although Fe systematically predominates over Mg in these phyllosilicates, consistent with previous reports (Perronnet et al. 2008; Mosser-Ruck et al. 2010). Except in reacted Garfield nontronite, two populations of 1:1 phyllosilicate particles were identified with contrasting crystallinity and crystal chemistry. In particular octahedral occupancies were much lower in Type II particles compared to Type I (2.25–2.26 and 2.73–2.77, respectively), whereas the iron oxidation state was much lower in the latter particle with $Fe^{3+}/\Sigma Fe$ ratios ranging from 0.44 to 0.46, compared to 0.70–0.78 for Type II particles. The 1:1 phyllosilicate resulting from the destabilization of Garfield nontronite had characteristics (e.g., octahedral occupancy and $Fe^{3+}/\Sigma Fe$ ratio) intermediate between those of the two types of particles.

The comprehensive description of the 1:1 phyllosilicates formed as the result of metallic iron-smectite interactions performed in the present study allowed refuting their description as "berthierine-like" species commonly found in previous reports often relying on little experimental support (Charpentier et al. 2006; Habert et al. 2006; Mosser-Ruck et al. 2010; Osacky et al. 2010; De Combarieu et al. 2011). Rather, cronstedtite and odinite are the 1:1 phyllosilicates to be considered for thermodynamical modeling relevant to the nuclear waste storage. More work is needed, however, to determine a possible crystallization sequence of these different Fe-rich 1:1 phyllosilicates as a consequence of smectite destabilization following the Ostwald step rule as suggested by Savage et al. (2010).

ACKNOWLEDGMENTS

J.-M. Bény (IST Orléans) and M. Jullien (CEA, Cadarache) are thanked for their valuable help with infrared spectroscopy and transmission electron microscopy. S.L. is grateful to F. Muller (IST Orléans) for insightful discussions.

REFERENCES CITED

Bailey, S.W. (1988a) Structures and compositions of other trioctahedral 1:1 phyllosiliactes. In P.H. Ribbe, Ed., Hydrous Phyllosilicates (exclusive of micas), 19, p. 169–188. Reviews in Mineralogy and Geochemistry, Mineralogical Society of America, Chantilly, Virginia.

——— (1988b) Odinite, a new dioctahedral-trioctahedral Fe^{3+}-rich 1:1 clay mineral. Clay Minerals, 23, 237–247.

Bauer, A., Lanson, B., Ferrage, E., Emmerich, K., Taubald, H., Schild, D., and Velde, B. (2006) The fate of smectite in KOH solutions. American Mineralogist, 91, 1313–1322.

Bildstein, O., Trotignon, L., Perronnet, M., and Jullien, M. (2006) Modelling iron-clay interactions in deep geological disposal conditions. Physics and Chemistry of the Earth, 31, 618–625.

Brandt, F., Bosbach, D., Krawczyk-Bärsch, E., Arnold, T., and Bernhard, G. (2003) Chlorite dissolution in the acid pH range: A combined microscopic and macroscopic approach. Geochimica et Cosmochimica Acta, 67, 1451–1461.

Brindley, G.W. (1982) Chemical compositions of berthierine—A review. Clays and Clay Minerals, 30, 153–155.

Charpentier, D., Devineau, K., Mosser Ruck, R., Cathelineau, M., and Villieras, F. (2006) Bentonite-iron interactions under alkaline condition: An experimental approach. Applied Clay Science, 32, 1–13.

Chermak, J.A. (1992) Low-temperature experimental investigation of the effect of high pH NaOH solutions on the Opalinus shale, Switzerland. Clays and Clay Minerals, 40, 650–658.

——— (1993) Low temperature experimental investigation of the effect of high pH KOH solutions on the Opalinus shale, Switzerland. Clays and Clay Minerals, 41, 365–372.

Claret, F., Bauer, A., Schafer, T., Griffault, L., and Lanson, B. (2002) Experimental investigation of the interaction of clays with high-pH solutions: A case study from the Callovo-Oxfordian formation, Meuse-Haute Marne underground laboratory (France). Clays and Clay Minerals, 50, 633–646.

Cuisinier, O., Masrouri, F., Pelletier, M., Villieras, F., and Mosser-Ruck, R. (2008) Microstructure of a compacted soil submitted to an alkaline PLUME. Applied Clay Science, 40, 159–170.

De Combarieu, G., Schlegel, M.L., Neff, D., Foy, E., Vantelon, D., Barboux, P., and Gin, S. (2011) Glass-iron-clay interactions in a radioactive waste geological disposal: An integrated laboratory-scale experiment. Applied Geochemistry, 26, 65–79.

Devol-Brown, I., Tinseau, E., Bartier, D., Mifsud, A., and Stammose, D. (2007) Interaction of Tournemire argillite (Aveyron, France) with hyperalkaline fluids: Batch experiments performed with powdered and/or compact materials. Physics and Chemistry of the Earth, 32, 320–333.

Egerton, R.F. (1996) Electron Energy-Loss Spectroscopy in the Electron Microscope, 485 p. Plenum, New York.

Farmer, V.C. (1974) The Infrared Spectra of Minerals, 539 p. The Mineralogical Society, London.

Gates, W.P., Slade, P.G., Manceau, A., and Lanson, B. (2002) Site occupancies by iron in nontronites. Clays and Clay Minerals, 50, 223–239.

Gates, W.P., Bouazza, A., and Churchman, G.J. (2009) Bentonite clay keeps pollutants at bay. Elements, 5, 105–110.

Geiger, C.A., Henry, D.L., and Bailey, S.W. (1983) Crystal structure of cronstedtite-$2H_2$. Clays and Clay Minerals, 31, 97–108.

Guggenheim, S., Bailey, S.W., Eggleton, R.A., and Wilkes, P. (1982) Structural aspects of greenalite and related minerals. Canadian Mineralogist, 20, 1–18.

Guillaume, D., Neaman, A., Cathelineau, M., Mosser Ruck, R., Peiffert, C., Abdelmoula, M., Dubessy, J., Villieras, F., Baronnet, A., and Michau, N. (2003) Experimental synthesis of chlorite from smectite at 300 °C in the presence of metallic Fe. Clay Minerals, 38, 281–302.

Guillaume, D., Neaman, A., Cathelineau, M., Mosser Ruck, R., Peiffert, C., Abdelmoula, M., Dubessy, J., Villieras, F., and Michau, N. (2004) Experimental study of the transformation of smectite at 80 and 300 °C in the presence of Fe oxides. Clay Minerals, 39, 17–34.

Habert, B., Jullien, M., Kohler, E., and Bonnin, D. (2006) Redox of iron in smectites. Clay Science, 12, 149–153.

Hamilton, D.L. and Henderson, C.M.B. (1968) The preparation of silicate compositions by a gelling method. Mineralogical Magazine, 36, 832–838.

Honty, M., De Craen, M., Wang, L., Madejova, J., Czimerova, A., Pentrak, M., Stricek, I., and Van Geet, M. (2010) The effect of high pH alkaline solutions on the mineral stability of the Boom Clay–Batch experiments at 60 °C. Applied Geochemistry, 25, 825–840.

Kodama, H. (1985) Infrared Spectra of Minerals: Reference guide to identification and characterization of minerals for the study of soils, 197 p. Technical bulletin 1985-1E, Agriculture Canada, Research Branch, Ottawa.

Kogure, T., Hybler, J., and Yoshida, H. (2002) Coexistence of two polytypic groups in cronstedtite from Lostwithiel, England. Clays and Clay Minerals, 50, 504–513.

Lantenois, S. (2003) Réacctivité fer métal/smectites en milieu hydraté à 80 °C, 226 p. Ph.D. thesis, Orléans University, France.

Lantenois, S., Lanson, B., Muller, F., Bauer, A., Jullien, M., and Plancon, A. (2005) Experimental study of smectite interaction with metal Fe at low temperature: 1. Smectite destabilization. Clays and Clay Minerals, 53, 597–612.

Moore, D.M. and Reynolds, R.C. Jr. (1997) X-ray Diffraction and the Identification and Analysis of Clay Minerals, 378 p. Oxford University Press, U.K.

Mosser-Ruck, R., Cathelineau, M., Guillaume, D., Charpentier, D., Rousset, D., Barres, O., and Michau, N. (2010) Effects of temperature, pH, iron-clay and liquid/clay ratios on experimental conversion of dioctahedral smectite to berthierine, chlorite, vermiculite, or saponite. Clays and Clay Minerals, 58, 280–291.

Osacky, M., Sucha, V., Czimerova, A., and Madejova, J. (2010) Reaction of smectites with iron in a nitrogen atmosphere at 75 °C. Applied Clay Science, 50, 237–244.

Perronnet, M. (2004) Réactivité des matériaux argileux dans un contexte de corrosion métallique: Application au stockage des déchets radioactifs en site argileux, 284 p. Ph.D. thesis, Institut National Polytechnique de Lorraine, France.

Perronnet, M., Jullien, M., Villieras, F., Raynal, J., Bonnin, D., and Bruno, G. (2008) Evidence of a critical content in Fe(0) on FoCa7 bentonite reactivity at 80 °C. Applied Clay Science, 38, 187–202.

Plançon, A. (2002) CALCIPOW—a program for calculating the diffraction by disordered lamellar structures. Journal of Applied Crystallography, 35, 377.

——— (2003) Modelling X-ray diffraction by lamellar structures composed of electrically charged layers. Journal of Applied Crystallography, 36, 146–153.

Ramirez, S., Vieillard, P., Bouchet, A., Cassagnabere, A., Meunier, A., and Jacquot, E. (2005) Alteration of the Callovo-Oxfordian clay from Meuse-Haute Marne underground laboratory (France) by alkaline solution. I. A XRD and CEC study. Applied Geochemistry, 20, 89–99.

Roux, J. and Volfinger, M. (1996) Precision measurements using a curved position-sensitive detector. Journal De Physique IV, 6, 127–134.

Sanchez, L., Cuevas, J., Ramirez, S., Riuiz De Leon, D., Fernandez, R., Vigil Dela Villa, R., and Leguey, S. (2006) Reaction kinetics of FEBEX bentonite in hyperalkaline conditions resembling the cement-bentonite interface. Applied Clay Science, 33, 125–141.

Savage, D., Walker, C., Athur, R., Rochelle, C., Oda, C., and Takase, H. (2007) Alteration of bentonite by hyperalkaline fluids: A review of the role of secondary minerals. Physics and Chemistry of the Earth, 32, 287–297.

Savage, D., Watson, C., Benbow, S., and Wilson, J. (2010) Modelling iron-bentonite interactions. Applied Clay Science, 47, 91–98.

Toth, T.A. and Fritz, S.J. (1997) An Fe-berthierine from a Cretaceous laterite: Part I. Characterization. Clays and Clay Minerals, 45, 564–579.

van Aken, P.A. and Liebscher, B. (2002) Quantification of ferrous/ferric ratios in minerals: new evaluation schemes of Fe $L_{2,3}$ electron energy-loss near-edge spectra. Physics and Chemistry of Minerals, 29, 188–200.

van Aken, P.A., Liebscher, B., and Styrsa, V.J. (1998) Quantitative determination of iron oxidation state in minerals using Fe $L_{2,3}$ electron energy-loss near-edge structure spectroscopy. Physics and Chemistry of Minerals, 25, 323–327.

Wilson, J., Cressey, G., Cressey, B., Cuadros, J., Ragnarsdottir, K.V., Savage, D., and Shibata, M. (2006a) The effect of iron on montmorillonite stability. (II) Experimental investigation. Geochimica et Cosmochimica Acta, 70, 323–336.

Wilson, J., Savage, D., Cuadros, J., Shibata, M., and Ragnarsdottir, K.V. (2006b) The effect of iron on montmorillonite stability. (I) Background and thermodynamic considerations. Geochimica et Cosmochimica Acta, 70, 306–322.

Zega, T.J., Garvie, L.A.J., and Buseck, P.R. (2003) Nanometer-scale measurements of iron oxidation states of cronstedtite from primitive meteorites. American Mineralogist, 88, 1169–1172.

Manuscript received November 25, 2011
Manuscript accepted February 7, 2012
Manuscript handled by Warren Huff